Corrosion Science 192 (2021) 109778

Contents lists available at ScienceDirect

Corrosion Science

journal homepage: www.elsevier.com/locate/corsci

A comparison of the corrosion behaviour of copper materials in dilute nitric acid

Anna Dobkowska [a,*], Millicent Dayle H. Castillo [a], Joseph P. Turnbull [a], Sridhar Ramamurthy [b], Dmitrij Zagidulin [a], Desmond E. Moser [c], Mehran Behazin [d], Peter G. Keech [d], David W. Shoesmith [a,b], James J. Noël [a,b]

[a] Department of Chemistry, The University of Western Ontario, London N6A 5B7, Canada
[b] Surface Science Western, The University of Western Ontario, London N6G 0J3, Canada
[c] Department of Earth Sciences, The University of Western Ontario, London N6A 5B7, Canada
[d] Nuclear Waste Management Organization, Toronto M4T 2S3, Canada

ARTICLE INFO

Keywords:
Copper
Acid corrosion
SEM
SIMS

ABSTRACT

The corrosion of a number of coarse- and fine-grained copper materials has been studied in an aerated aqueous nitric acid (100 mM) solution. The materials properties and the consequences of corrosion were characterized by scanning electron microscopy, electron back scatter diffraction and confocal laser scanning microscopy. The corrosion of the coarse-grained materials was shown to be strongly influenced by the crystallographic orientations of grains. For fine-grained materials grain boundary etching at high angle grain boundaries and grain boundary pores (for cold sprayed copper) overrode the influences of texture on the corrosion rate.

1. Introduction

The microstructure of polycrystalline materials often has an important influence on corrosion, as has been widely described in the literature [1–8]. Corrosion initiation is commonly controlled by metallurgical factors and the inhomogeneity of structures, with the subsequent propagation mostly controlled by kinetic factors (i.e., polarization and diffusion) [9–11]. A number of studies have been devoted to investigating the effect of grain-size on corrosion of face-centered cubic (fcc) metals [3,12–20], and a review of this literature shows that the corrosion resistance improves with a reduction in grain size from coarse-grained (CG) to nanocrystalline (NC). Since grain boundaries can act as corrosion barriers, the more refined the microstructure, the higher the expected overall corrosion resistance [13,21].

An interesting insight into microstructure-dependent corrosion of metals was made by Gollapudi [22], who showed that, in a non-passivating environment, a bimodal microstructure with a higher volume fraction of coarse grains may increase the corrosion resistance of metals. These systematic studies were carried out to find the relationship between grain refinement and corrosion rate for fcc-structured metals. However, this relationship may be disrupted by other microstructural factors such as crystallographic orientation, grain boundary distribution, discontinuities (voids or pores), or internal stress/strain that may be introduced into the material during fabrication or post-processing. Studies on the influence of grain orientation on corrosion [23–31] prove that differences in the electrochemical behaviour of grains in coarse-grained, fine-grained, and nanocrystalline materials are related to differences in the crystallographic orientations. Martinez-Lombardia et al. [23] found that for Cu in the active state, $<111>$ //ND grains were the most reactive which is counter to expectations based on surface energies and work functions. It was also shown that the reactivity of $<100>$ //ND grains decreased when located between $<111>$ //ND grains, an observation consistent with those of Lapeire et al. [24].

The grain boundary misorientation angle also plays an important role in determining the corrosion resistance; with grain boundaries possessing a misorientation angle higher than 15° corroding faster than those with a misorientation angle below 15° [8,16,32]; i.e., the effect of the "special" coincidence site lattice (CSL) boundaries is a key feature [26,33–37]. It has been suggested that for low stacking fault fcc-structured metals, a higher fraction of low-Σ CSL boundaries may enhance the corrosion resistance, especially for intergranular corrosion [33,35]. A new insight into the influence of grain boundary properties on Cu corrosion is given by Chen et al. [27], who showed that a thicker

* Corresponding author.
E-mail address: anna.dobkowska@pw.edu.pl (A. Dobkowska).

https://doi.org/10.1016/j.corsci.2021.109778
Received 23 March 2021; Received in revised form 13 August 2021; Accepted 14 August 2021
Available online 17 August 2021

passive film was formed at random grain boundaries than at coherent twin boundaries. The effect of the porosity on the corrosion resistance of fcc-structured Cu produced by cold spray deposition has also been investigated. [38], but there is a lack of evidence showing how changes in local chemistry within pores influences corrosion reactions.

The resistance of polycrystalline fcc metals to corrosion is complex and involves a number of factors for which a complete understanding has not yet been realized. Most notably the consideration of texture and grain size distribution becomes important when designing long-lived structures such as used fuel containers (UFC) for the permanent disposal of high-level nuclear waste. The UFC is a key barrier in the multi-barrier systems proposed in Canada and many other countries for the long-term containment and isolation of used nuclear fuel in a deep geologic repository (DGR). In the proposed Canadian design, used nuclear fuel will be sealed in UFCs fabricated from carbon steel vessels (ASME SA516 Gr.70) covered with an approximately 3 mm-thick Cu coating, applied by electrodeposition and cold spray deposition techniques [39,40]. For the large majority of their lifetime in a DGR, the UFCs will be exposed to anoxic conditions. However, for a brief initial period after emplacement, oxygen will be present in the DGR, trapped within the filling and sealing materials during UFC emplacement. During this relatively short period, which may last from a few weeks to a few decades, oxides of Cu may be present on the surface of the UFC [41]. An understanding of the early, oxygen-initiated corrosion behaviour of the Cu coating is important to ensure safe, long-term disposal [42–46], although the range of oxic damage is expected to be only on the order of tens or hundreds of micrometres.

As noted above, a range of evolving exposure conditions is anticipated over the lifetime of a DGR (i.e., 1 million years). Reviews by King et al. [47] and Hall et al. [48] summarize the current understanding of container corrosion behaviour as DGR conditions evolve. In the early stages of container emplacement in a DGR, warm, humid air conditions could prevail, and with a current Canadian container thinner than those of previous container designs, gamma radiation fields on the outer surface of the container could be more significant. This could lead to the production of small amounts of HNO_3 by the radiolysis of aerated vapour [49,50], which may lead to small amounts of corrosion. The kinetics of this corrosion process have been studied by Turnbull et al. [51–53].

The current work compares the influence of metallurgical features such as grain size, grain distribution and the crystallographic orientations of grains, on the corrosion behaviour of pure Cu materials fabricated by various techniques. To determine how these microstructural features could influence corrosion, the extent and distribution of corrosion damage on Cu specimens after exposure to aerated HNO_3 solution were analysed.

2. Materials

Five different Cu materials were examined in this work: P-doped O-free wrought Cu (SKB Cu), electrolytic tough pitch Cu (ETP Cu), commercial wrought Cu (CW Cu), electrodeposited Cu (ED Cu), and cold spray deposited Cu (CS Cu).

The SKB Cu is a P-doped O-free wrought Cu supplied by the Swedish Nuclear Fuel and Waste Management Company (SKB, Solna, Sweden). The ETP Cu, in the form of a plate (30 cm × 30 cm × 0.5 cm), was purchased from Rolled Alloys Inc., Mississauga, Canada, and the CW Cu was a typical commercially available Cu plate material (10 cm × 3 cm × 0.5 cm, manufacturer unknown). The ED Cu was supplied in the form of a 3-mm-thick Cu coating on a 15 cm × 15 cm × 0.4 cm A516 Gr. 70 steel block substrate, by Integran Technologies Inc., Mississauga, Canada. The CS Cu was manufactured by the National Research Council of Canada, Boucherville, Canada, also in the form of a 3-mm coating on a steel substrate (A516 Gr. 70). The CS Cu was annealed at 350 °C for 1 h after deposition to relieve stresses [42,43,54].

3. Experimental methodology

3.1. Microstructural characterization

The microstructure of each material was examined by electron backscatter diffraction (EBSD) in the Zircon and Accessory Phase Laboratory, The University of Western Ontario, using a Hitachi S6600 scanning electron microscope (SEM) equipped with an Oxford Symmetry Nano EBSD detector. Cu coupons were mounted in an epoxy resin, ground with SiC papers (#600, #1200, #2500 and #4000), and then polished using 3 and 1 μm diamond suspensions in a glycol-based lubricant. Specimens were ultrasonically rinsed in methanol before electropolishing at room temperature using an electrolyte composed of HNO_3:CH_3OH = 1:3 by volume (HNO_3, ACS reagent, 68–70%; CH_3OH, ACS reagent). Using a GPR-H Series Linear D.C. Power Supply, a voltage of 10 V was applied for 10 s to specimens immersed in this solution. Prior to transfer to the SEM chamber, the surface of the specimens was flat-milled with an Ar ion beam for 6 min, using an IM4000 Hitachi Plus Ion Milling System. The EBSD data were acquired using AZtecHKL software (Oxford Instruments NanoAnalysis Group). Measurements were performed with a step scan of 0.5 μm and a working distance of 22.3 mm. The recorded data were analyzed using Oxford HKL Chanel 5 software. The orientation images are shown as inverse pole figure (IPF) maps. In a polycrystalline material, two types of grain boundaries (GBs) can be distinguished. If the angle between two adjacent grains is below 15°, then the GBs are defined as low-angle grain boundaries (LAGBs) and marked in green in IPF maps. If the neighboring grains are misoriented by more than 15°, then the GB is defined as a high-angle grain boundary (HAGB) and marked in red in the IPF maps. Non-indexed areas are marked in black. The IPF maps and corresponding GB distributions obtained are shown after the processing, except for the data acquired for CS Cu which is presented in its original form.

To determine the average grain size and the relative frequency of grain sizes, we used a post-processing procedure involving a grain tolerance angle of 2° and a cut-off limit of 10 pixels. The grain size was determined using a linear intercept method. To estimate the variation in grain sizes, the coefficient of variation (C_v) was calculated using the following formula:

$$C_v = \frac{\sigma}{\mu}$$

where σ is the standard deviation and μ is the average grain size dimension.

To further determine the microstructure of CS Cu, SEM observations were performed on the same specimen used for EBSD measurements. The images were captured using a Hitachi S4500 field emission SEM. Dynamic secondary ion mass spectrometry (D-SIMS) was performed to determine whether oxygen was present between splats of CS Cu. Measurements were performed using a Cameca IMF-6f SIMS and an area of 250 μm × 250 μm was sputtered.

The microstructure of SKB Cu was additionally observed using an optical microscope (6000 VHS Keyence), after polishing and chemical etching using 20 mL NH_4OH + 20 mL H_20 + 10 mL 3% H_2O_2.

3.2. Electrochemical corrosion tests

For electrochemical measurements specimens with the dimensions 1 cm × 1 cm x 0.5 cm were cut from plate materials, tapped, threaded, and connected to steel rods covered with PTFE heat-shrink tubing. Specimens were ground with SiC papers (#600, #1200, #2500 and #4000) and polished with 3 and 1 μm diamond suspensions in a glycol-based lubricant. Prior to each electrochemical measurement, specimens were rinsed with Type-1 water, ultrasonically cleaned in methanol, and then dried with high purity Ar gas.

In this study experiments were conducted in solutions containing

100 mM HNO_3 to investigate the accelerated corrosion of copper surface exposed to maximum accumulated concentration of HNO_3 anticipated in a DGR [55], and also to facilitate the comparison with previous studies. The E_{corr} was recorded as a function of immersion time. After 24 h of immersion of coupons in an aerated HNO_3 solution, the polarization resistance (R_p) of each specimen was determined by linear polarization resistance (LPR) measurements performed over a potential range of $E_{corr} \pm 5$ mV, at a scan rate of 10 mV/min. Experiments were performed in a large volume, three-compartment electrochemical cell. A saturated calomel electrode (SCE) was used as the reference electrode (RE), a Pt wire as a counter electrode (CE), and a polished Cu specimen with 1 cm^2 of exposed area as a working electrode (WE). All electrochemical measurements were performed using a Solartron Analytical Modulab. The 100 mM HNO_3 solution was prepared using HNO_3 stock solution (ACS reagent, 68–70%, Fisher Scientific) and Type-1 water (18.2 MΩ·cm). To ensure the reproducibility of the results the experiments were repeated at least twice.

3.3. Characterization of corroded surfaces

After electrochemical measurements specimens were examined using a Hitachi SU3500 Variable Pressure SEM. The surface topography was measured and depth profiling of corroded surfaces performed using confocal laser scanning microscopy (CLSM, Zeiss LSM800 For Materials). The collected data are shown in the form of 3D images, with the attached colour scale indicating depth, and as surface profiles. In depth profiling, the deepest point detected by CLSM was adopted as zero on the ordinate (depth) axis. Imaging was performed with a 405-nm excitation laser. All measurements were performed with a 0.2 μm interval between slices. Quantitative analyses of surface profiles were based on measurements of the arithmetic mean height (S_a) and maximum height (S_z), where S_a describes the mean surface roughness, and S_z the height difference between the highest peak and the deepest valley within the analyzed area [56].

4. Results

4.1. Microstructural characterization

An optical image, IPF map and GB distribution for a polished and etched SKB Cu surface are shown in Fig. 1. As observed in Fig. 1a, the microstructure is characterized by coarse grains with an average size of 29 μm. The grains are randomly oriented, and almost all detected GBs reside between grains whose orientation differs by more than 15°, Fig. 1b. (Note that, due to the large grain size and the low number of grains within the field of view, the grain size distribution for this material is not shown in Fig. 3 with those of the other materials). A detailed characterization of the microstructure of SKB Cu has been published by Li et al. [57].

ETP Cu has a random texture and exhibits a heterogeneous microstructure comprised of grains of different sizes, Fig. 2, with the majority of grain boundaries being HAGBs, Fig. 2b. The distribution of grain sizes, Fig. 3, shows that grains with an equivalent dimension below 5 μm comprise 55% of the analyzed population, and those with an equivalent dimension between 5 and 10 μm make up 31% of the population. Bigger grains contribute much smaller fractions of the population. The average grain size was estimated to be 6.1 μm, with a C_v value of 0.8.

Of the materials analyzed, CW Cu has the broadest grain size distribution, as indicated by a C_V value of ~ 1, with randomly oriented grains with an average size of 7.8 μm, Fig. 3 and Fig. 4a. HAGBs are present but LAGBs are still observed, Fig. 4b. Grains measuring below 5 μm make up 55% of all analyzed grains, with those between 5 and 10 μm comprising 20%, Fig. 3. Grains with larger sizes are also present, but in only minor amounts.

The ED Cu has a well-refined microstructure, Fig. 5, with an average grain size of 2.8 μm, Fig. 3, with the C_v value of 0.4 indicating only a small variation in grain size. Of the analyzed population, 94% of grains have an equivalent dimension below 5 μm, with those between 5 and 10 μm comprising 6% of the population. As shown by the dominance of blue and green regions, respectively, in the IPF map, Fig. 5a, the vast majority of the grains are oriented to (111) and (101). The grains oriented to (001) are smaller, and randomly distributed within the whole analyzed area. Mostly HAGBs were formed, Fig. 5b. Such a refined microstructure would provide greater strength in the Cu coating, which is critically important in optimizing the mechanical properties of the UFC [57,58].

The most refined microstructure, with an average grain size of 2.7 μm, was observed in CS Cu. During the low temperature annealing, recrystallization occurred [43,59], and ultrafine and nearly equiaxed grains were formed, Fig. 6a. The grain size in CS Cu is reasonably homogeneous (C_v ~ 0.4), Fig. 3. As observed for ED Cu, the smallest grains, with an equivalent dimension below 5 μm, comprised the great majority of the analyzed population (95%), with the remainder between 5 and 10 μm. HAGBs were formed around recrystallized grains, but compared to ED Cu, a significantly larger number of LAGBs are present, Fig. 6b.

The indexation rate from EBSD data was 77%, with the vast majority of the non-indexed fraction due to the presence of microstructural defects (pores formed during deposition) [43]. Within the structure, pores can be observed, Fig. 7a. The observed pores can be classified according to their different shapes. Large pores, located at triple points, Fig. 7b, are around 4 μm in size. The depth of several randomly selected pores was approximately measured by subtraction of the working distance of the microscope measured when focusing on the bottom of the pore from that measured when focusing on the surface. This yielded pore depths in the

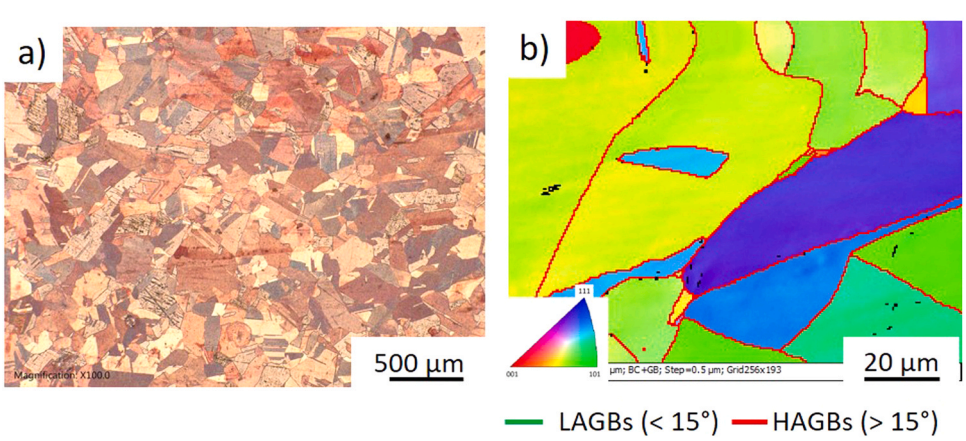

Fig. 1. Microstructure of SKB Cu; a) optical image after chemical etching; b) IPF map with corresponding GB distribution.

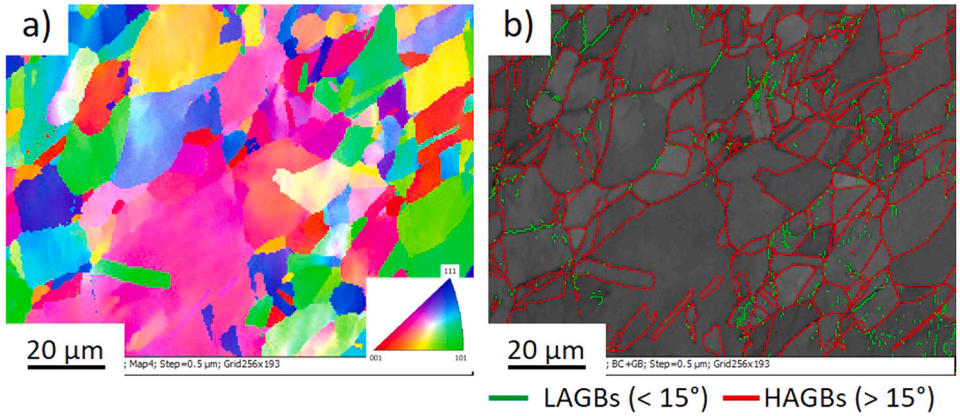

Fig. 2. EBSD maps recorded on the surface of ETP Cu: a) IPF map, b) GB distribution.

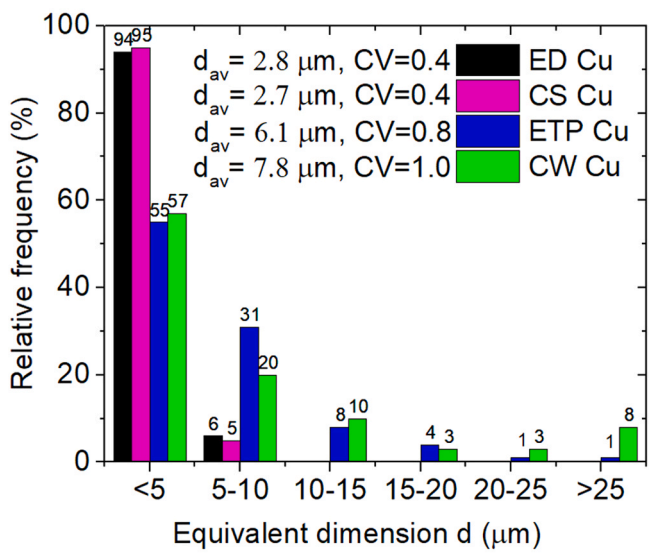

Fig. 3. Grain size distribution in different Cu materials, estimated using the linear intercept method.

range 20–46 µm. Pores in CS Cu coatings deposited on steel have been observed previously by Yu et al. [59] and Li et al. [57]. Both studies focused on the negative influence of randomly distributed pores in CS Cu on the mechanical properties of the Cu coating.

SEM imaging showed long pores that extended along the length of several adjacent particles located at particle boundaries, Fig. 7c, indicating weakly bonded particle-particle interfaces. Although low temperature annealing was used to minimize the porosity (350 °C for 1 h), weakly bonded areas were still present in the coating, indicating that conditions used during cold spray deposition and annealing did not lead to the complete sintering of the inter-splat areas [59]. Small grains are visible in the particle interiors suggesting that microstructural recrystallization occurred Fig. 7d; however, further studies regarding the detailed microstructure recrystallization should be undertaken.

4.2. Corrosion measurements

E_{corr} measurements recorded in aerated 100 mM HNO_3 for 24 h are shown in Fig. 8. The evolution in E_{corr} on SKB Cu and ED Cu exhibited similar trends, a rapid, initial decrease followed by a slower longer-term increase. The initial E_{corr} decrease on ED Cu was more rapid than on SKB Cu, with the minimum potential achieved lower (~ −0.05 V/SCE) than that on SKB Cu (−0.04 V/SCE to −0.03 V/SCE). The ETP Cu and CW Cu also exhibited similar behaviors but were different from SKB Cu and ED Cu, with the initial decrease in E_{corr} followed by a steady increase towards steady-state values of ~ 0.03 V/SCE (CW Cu) and ~ 0.05 V/SCE (ETP Cu). The CS Cu exhibited very different behavior, initially rising to ~ 0.07 V/SCE before decreasing slowly to ~ 0.03 V/SCE, a value in the same range as achieved with CW Cu and ETP Cu.

After 24 h of exposure, when E_{corr} approached a constant value, R_p measurements were collected, Table 1. The apparent corrosion rate ($\propto R_p^{-1}$) was highest on CS Cu, considerably lower on ED Cu, and of intermediate range on SKB Cu, ETP Cu and CW Cu. Moreover, all the longer-term values (i.e., after 24 h of immersion) are in the range

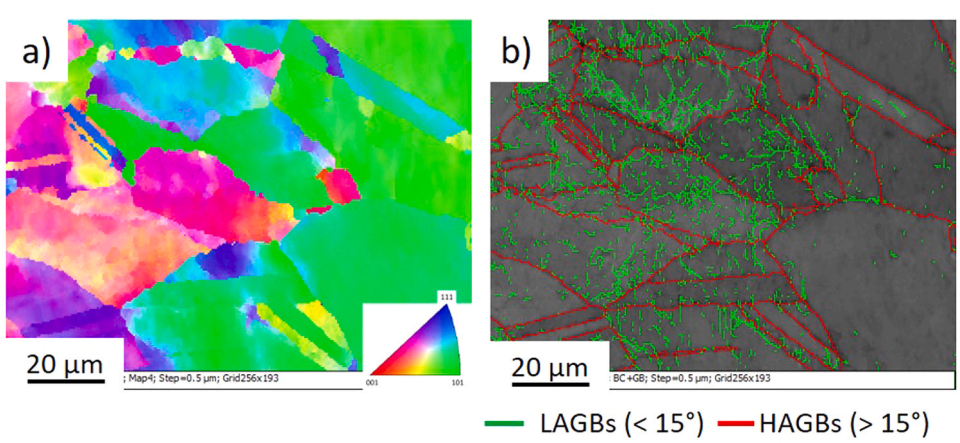

Fig. 4. EBSD maps recorded on the outer surface of CW Cu: a) IPF map, b) GB distribution.

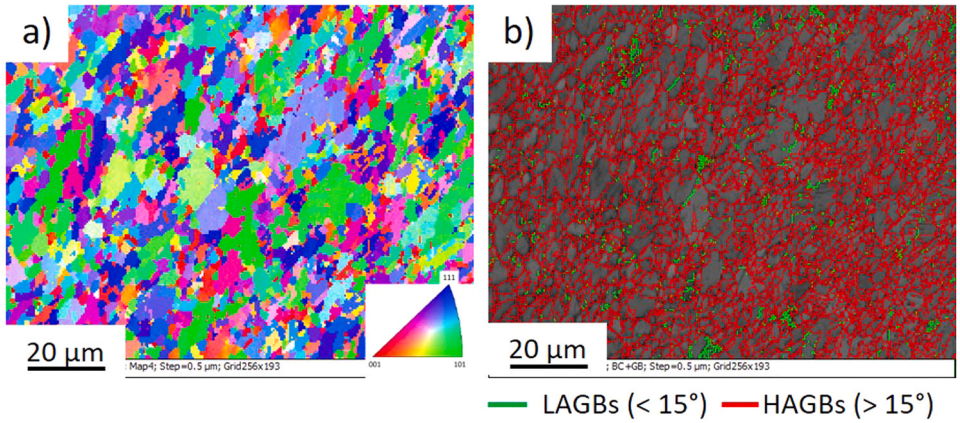

Fig. 5. EBSD maps recorded on the outer surface of ED Cu coating: a) IPF map, b) GB distribution.

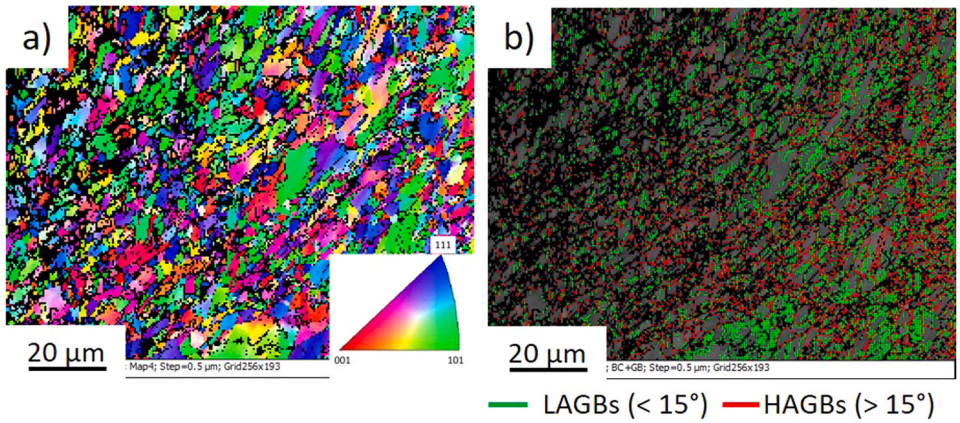

Fig. 6. EBSD maps recorded on the outer surface of CS Cu coating: a) IPF map, b) GB distribution.

(0.04 V/SCE to −0.04 V/SCE) which we have observed in many experiments conducted in HNO_3 solutions in the HNO_3 concentration range 10–150 mM [60]. No apparent relationship between E_{corr} and R_p was observed, suggesting that the differences in R_p cannot be explained by a simple rebalancing of the relative rates of the anodic and cathodic reactions.

4.3. Characterization of corroded surfaces

Fig. 9 shows that corrosion damage in aerated nitric acid was non-uniformly distributed on SKB Cu, with some grains experiencing more extensive corrosion than others. These differences were confirmed in the 3D CLSM image in Fig. 10a with the variations in depths of corrosion on individual grains shown in Fig. 10b. Measurements made on areas such as the one shown in Fig. 10a show that both S_a and S_z were greater on grain A than on grain B, Fig. 9a–c. In addition, if two adjacent grains have the same etch patterns after exposure in the test solution, then it can be supposed their exposed surfaces have similar crystallographic orientation, leading to preferential corrosion of HAGBs (Fig. 9c and d).

Examination of ETP Cu showed a texture-dependent corrosion pattern similar to that of SKB Cu, as indicated by grains A, B and C in Fig. 11a. The 3D map in Fig. 11b and the surface profile in Fig. 11c show the differences in grain etching reflecting the much lower average grain size in ETP Cu. Similar texture-dependent corrosion was observed on CW Cu, Fig. 12a–c. This is not unexpected, given similarities in their grain size distributions, Fig. 3, except for the small number of large grains present in CW Cu. Both the surface roughness (S_a) and corrosion depth (S_z) on CW Cu were approximately twice the values observed on ETP Cu, which may reflect the approximate doubling in the corrosion rate of CW Cu compared to that of ETP Cu (Table 1). The SEM and CLSM images and a surface profile for ED Cu are shown in Fig. 13. Corrosion damage appeared to be greatest along grain boundaries, with the frequency of deeper penetrations indicated in the surface profile consistent with the average grain size. Since this specimen has a relatively high density of HAGBs, Fig. 5b, it was likely that corrosion initiated at these locations with the surface profile, Fig. 13c, and higher S_z value suggesting that it remained dominantly concentrated in these locations. Despite this localization of corrosion, the mean roughness (S_a) of the ED Cu remained similar to those of the ETP Cu and CW Cu. In addition, despite the high density of corrosion-susceptible HAGBs, R_p for the ED Cu was 3–5 times higher than those of ETP Cu and CW Cu, respectively.

Examination of the corroded specimens showed that corrosion in aerated nitric acid solution was more localized on CS Cu (Fig. 14) than on the other specimens and propagated along preferential pathways. The shape and distribution of these corroded locations indicated that the most corrosion-susceptible areas were located at the pores and along the particle boundaries present in this material, Fig. 7. The CLSM surface profile showed the deepest penetrations at these locations, Fig. 14d. The maximum corrosion penetration measured in the area shown in Fig. 14b was 80 µm, which is considerably greater than the penetration depths measured on the other specimens. Dynamic SIMS mapping by ^{16}O showed that the particle boundaries were rich in O, Fig. 14c. This was most likely due to surface oxidation of the Cu particles used in the deposition process, which was retained at the particle boundaries. To examine the corrosion damage, a CLSM map and surface profile were recorded on the area marked with the black square in Fig. 14b and are

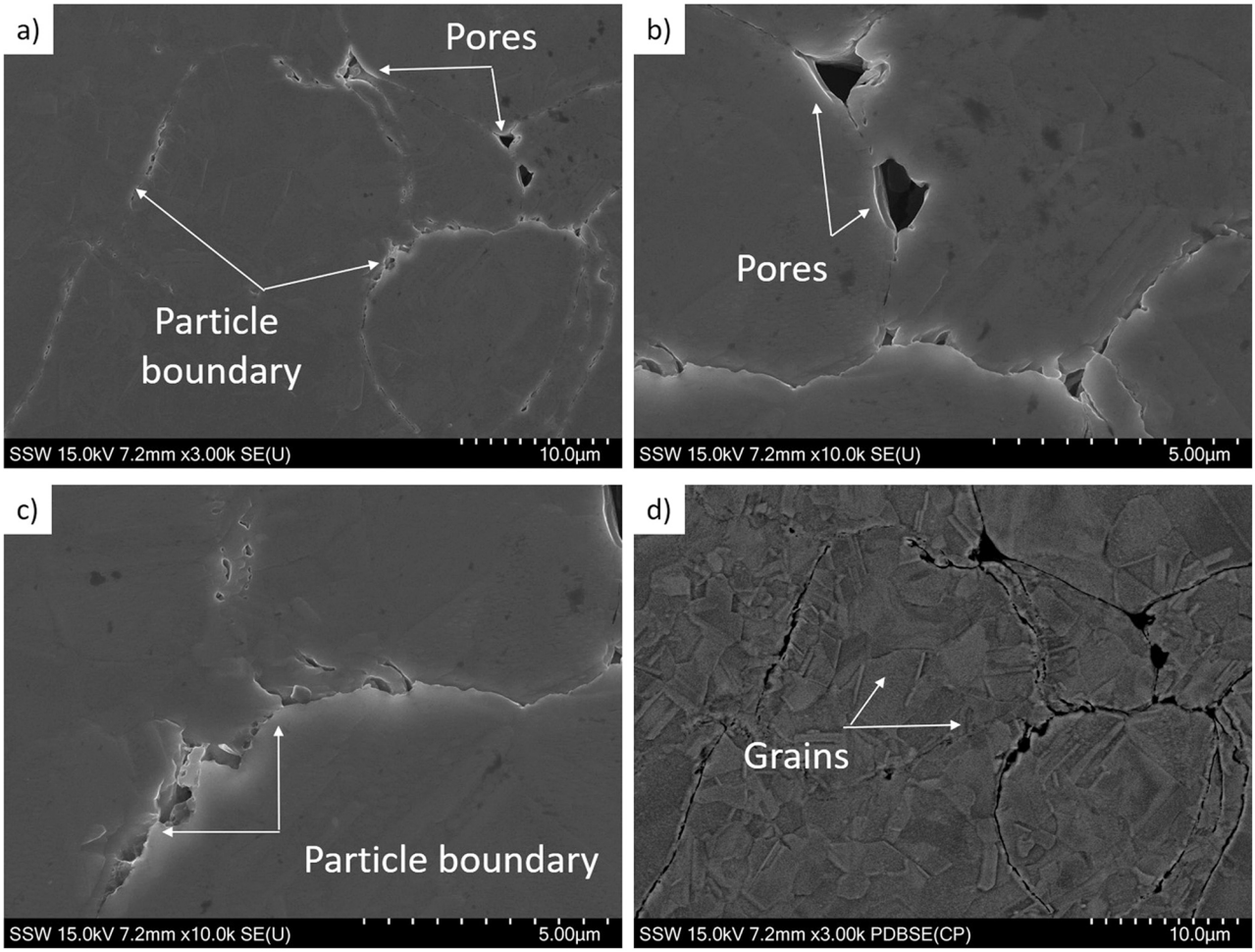

Fig. 7. SEM images recorded on the surface of the CS Cu specimen prepared for EBSD measurements: a) overall SE image, b) SE image highlighting the location of pores, c) weakly bonded particle-particle interfaces, d) BSE image taken from the same area as image 7a.

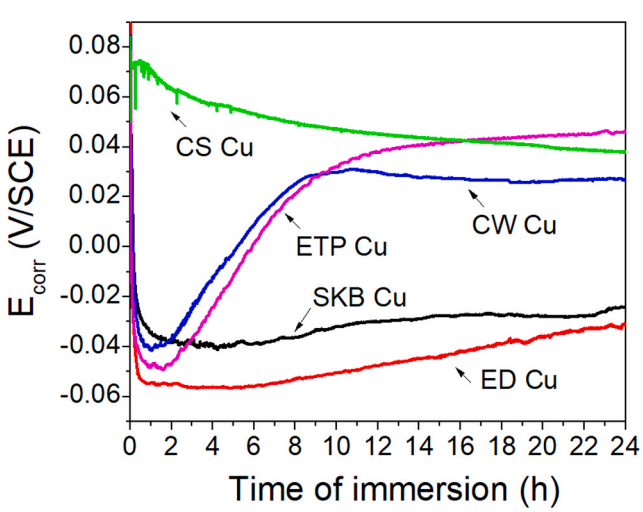

Fig. 8. E_{corr} evolution as a function of time of immersion in aerated 100 mM HNO_3.

shown in Fig. 15. The S_a and S_z values within this 70 µm × 70 µm area are 1.7 µm and 10 µm, respectively. Corrosion damage to the central part of a deposit particle is shown in Fig. 16.

Table 1
R_p measurements after 24 h of immersion in aerated 100 mM HNO_3.

Material	Linear polarization R_p (Ω·cm^2)
ED Cu	2269
ETP Cu	712
SKB Cu	569
CW Cu	469
CS Cu	49[a]

[a] due to an increasing effective area, the value may only be approximate

5. Discussion

The Cu specimens investigated in this study can be separated into coarse-grained (SKB Cu, ETP Cu, CW Cu) and refined grain (ED Cu, CS Cu) materials.

5.1. *The major factors affecting the corrosion behaviour of coarse-grained Cu*

The key features controlling the corrosion of the coarse-grained materials were the crystallographic orientation of grains, with variously oriented grains corroding at different rates. The rates for all 3 specimens were within a factor of 2 (Table 1), with the E_{corr} for the very large grained SKB Cu substantially lower than that for the ETP Cu and CW Cu. Miyamoto et al. [9] suggested that this dependence on texture

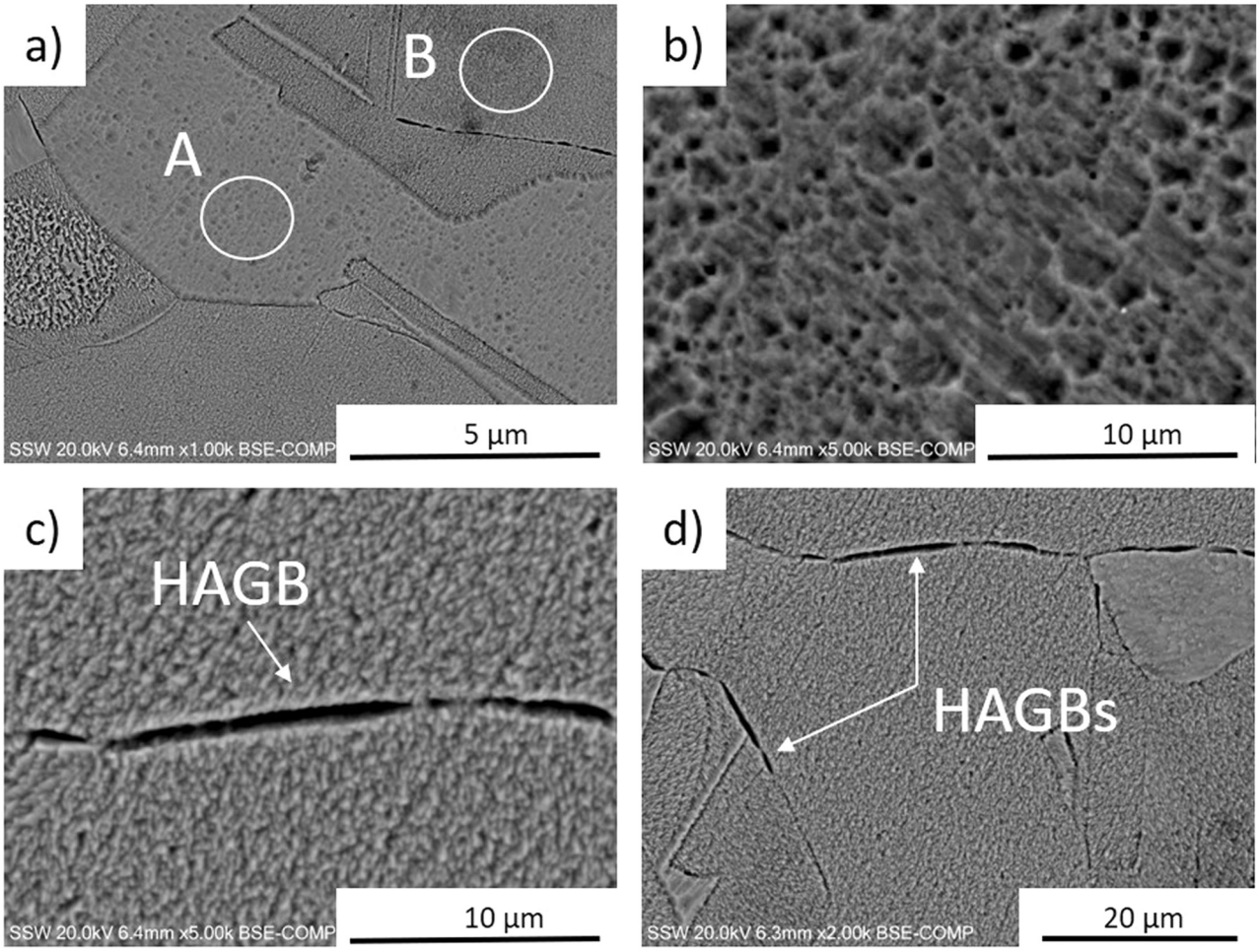

Fig. 9. SEM images of the surface of SKB Cu after immersion in HNO_3 for 24 h. Areas A and B are shown with higher magnification in Fig. 9b and c, respectively. Panels c and d show preferential etching of HAGBs.

can be assigned to the establishment of anodic/cathodic separation between individual grains. They proposed that this could result from differences in surface energies between crystal planes, with the close packed < 111 > plane having the lowest surface energy. Subsequently, Lapeire et al. [13] demonstrated that not only the grain orientation but also the orientation of neighbouring grains exhibited an influence on the corrosion behaviour of specific grains, and suggested that the greatest degree of galvanic coupling between grain interiors would be between < 001 > // ND and < 111 > // ND oriented grains, particularly if they were located adjacent to each other [24]. How this leads to the rebalancing of the anodic and cathodic kinetics, which would account for the lower E_{corr} for SKB Cu, is presently unclear. The variation of corrosion rate with texture will also be complicated by anion adsorption processes, which could be particularly important in NO_3^- solutions, since this anion has been shown to have different adsorption energies on different crystal planes [61].

In addition, within this group of coarse-grained materials, the very large grained SKB Cu exhibited preferential grain boundary etching of HAGBs. The higher energies at these locations make them preferential corrosion sites relative to the lower energy grain surfaces, as described by Miyamoto et al. [9], this leads to a combination of GB etching and the more visible etching of the more sensitive crystallographic planes. Miyamoto et al. [9] went on to propose that the mechanism for this effect was a type of galvanic coupling between the grains and grain boundaries.

Our results are not inconsistent with the results of Miyamoto et al. [9] and Lapeire et al. [13], and it is possible that an intra-microstructural-feature galvanic corrosion mechanism may be responsible, though we do not yet have direct evidence for the anode-cathode separation that would confirm it.

5.2. *The major factors affecting the corrosion behaviour of fine-grained Cu*

A number of studies [16,37,62–65] have demonstrated the enhanced reactivity of HAGBs, with the corrosion rate depending on their number and distribution. However, despite the extremely high number and density of such boundaries, ED Cu was the most corrosion resistant of these materials, exhibiting a R_p value 3–6 times greater than the values recorded for the other 4 materials (Table 1). This decrease in corrosion rate, combined with a lower E_{corr} (compared to the other materials), indicates a suppression of the cathodic reaction on the ED Cu surface. Miyamoto et al. proposed that the dominant influence on the corrosion rate of fine-grained Cu is galvanic coupling between the grains, acting dominantly as cathodes, and the HAGBs which act dominantly as anodes [9]. In this scenario, a refined structure containing dominantly HAGBs will possess a low cathode (grain surface) area to anode (HAGBs) area ratio which, while dominantly supporting corrosion within the HAGBs, would limit the overall rate of corrosion penetration. That HAGB etching was observed for the large-grained SKB Cu (large ratio of grain interior to grain boundary surface area) but not the smaller-grained ETP Cu and CW Cu (smaller grain interior: grain boundary area ratio) is also in line with the results of Miyamoto et al. [9].

For the CS Cu, corrosion propagated preferentially within the

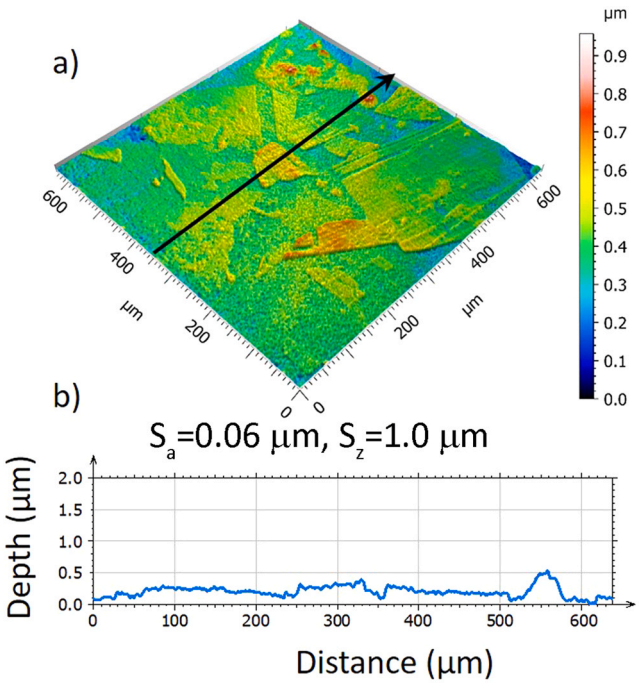

Fig. 10. CLSM image recorded on the surface of SKB Cu: a) 3D image, b) surface profile extracted from the location marked by the arrow.

particle boundaries. Despite a lower density of HAGBs than on ED Cu and a similar small grain size, the corrosion rate and E_{corr} for CS Cu were both considerably higher than those of ED Cu. This indicates faster cathodic reaction kinetics on the former than the latter material. The E_{corr} of CS Cu was approximately the same as that of the coarse-grained materials but the corrosion rate was considerably higher, a combination suggesting that both the anodic and cathodic reaction kinetics were faster on CS Cu. Although annealing has been shown to significantly decrease plastic strain within the interparticle boundaries [42], it is possible that small amounts of residual strain exerted an influence on the anodic kinetics. These observations demonstrate that any influence of inter-microstructural-feature galvanic coupling was overridden by the enhanced overall cathodic and anode reaction kinetics on CS Cu.

5.3. Corrosion mechanism

The mechanism of Cu corrosion in aerated HNO_3 has been shown to be complicated [52,53,60]. Nitrate is strongly adsorbed on Cu [61] and, in the absence of dissolved O_2, prevents corrosion either due to NO_3^- adsorption or to the formation of a protective oxide [53,61]. When dissolved O_2 is present it acts as the dominant oxidant,

$$O_2 + 4H^+ + 4e^- \rightarrow \quad 2H_2O \tag{1}$$

leading to the overall corrosion reaction,

$$O_2 + 4Cu \quad + \quad 4H^+ \quad \rightarrow 4Cu^+ + \quad 2H_2O \tag{2}$$

with the overall reaction kinetics being first-order with respect to $[O_2]$ but independent of $[H^+]$ and only slightly dependent on $[NO_3^-]$ [52,53,66]. These studies also demonstrated that corrosion supported by H^+ reduction does not occur. The Cu^+ produced in reaction 2 can then undergo competitive homogeneous oxidation reactions:

$$4Cu^+ + 2O_2 + 4H^+ \rightarrow 4Cu^{2+} + 4OH^- \tag{3}$$

and

$$NO_3^- + \quad 2Cu^+ + 2H^+ \rightarrow NO_2^- + 2Cu^{2+} + \quad H_2O \tag{4}$$

Reaction 4 effectively activates NO_3^- as an oxidant, since the NO_2^- formed acts as a rapid cathodic reactant [52],

$$NO_2^- + 2H^+ + e^- \rightarrow NO + H_2O \tag{5}$$

supporting the overall corrosion reaction

$$NO_2^- + Cu + \quad H^+ \rightarrow NO + Cu^+ + \quad OH^- \tag{6}$$

with the Cu^+ produced in reactions (2) and (6) consumed by reactions (3) and (4) to produce Cu^{2+} whose reduction on the Cu surface leads to further corrosion via comproportionation reaction (7),

$$Cu + \quad Cu^{2+} \quad \rightarrow 2Cu^+ \tag{7}$$

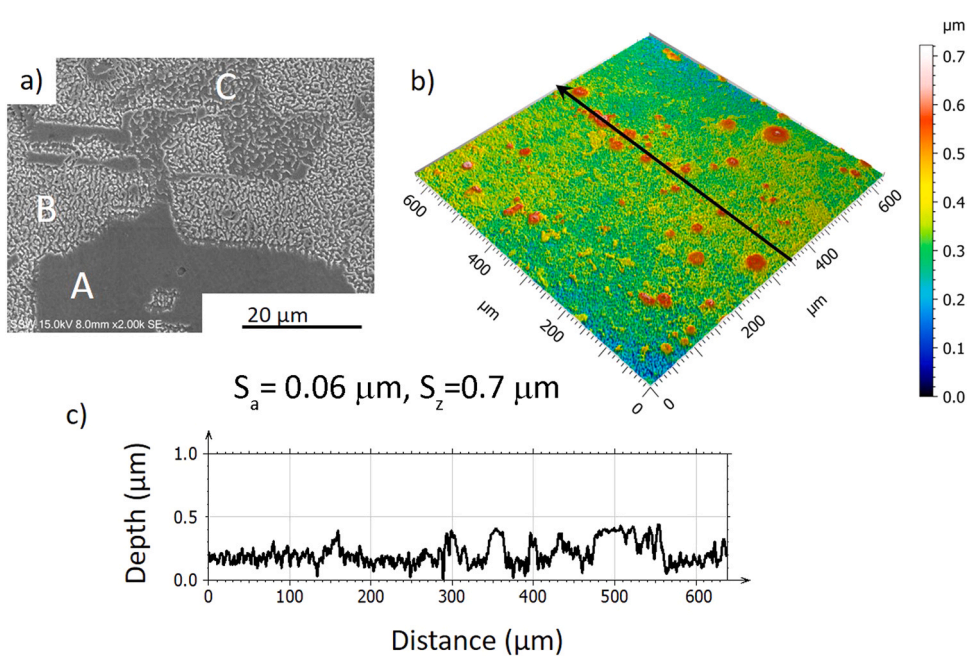

Fig. 11. Post-corrosion characterization of ETP Cu: a) SEM image, b) CLSM 3D image, d) surface profile extracted along the location marked by the arrow.

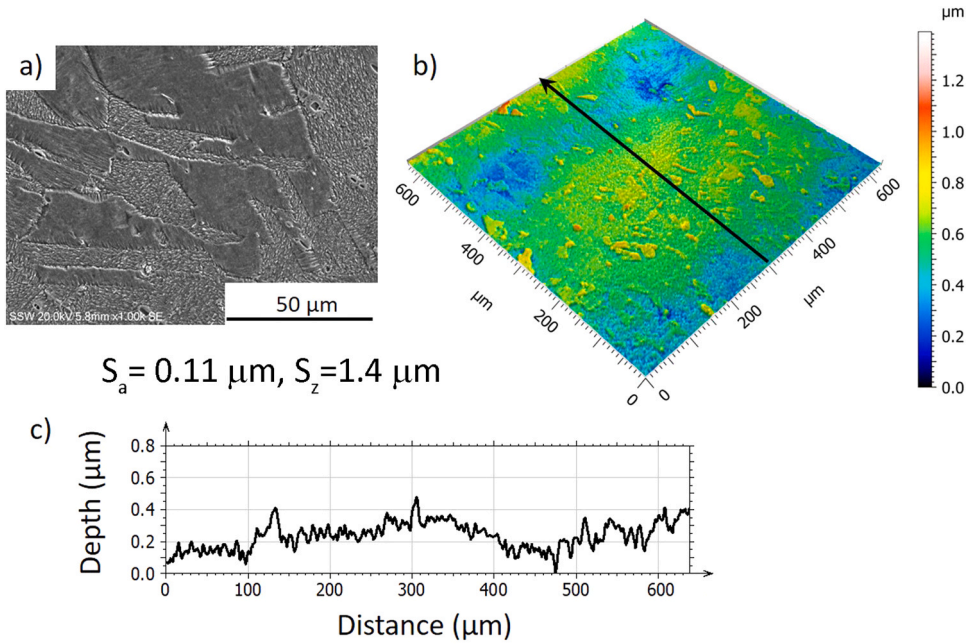

Fig. 12. Post-corrosion characterization of CW Cu: a) SEM image, b) CLSM 3D image, d) surface profile extracted along the location marked by the arrow.

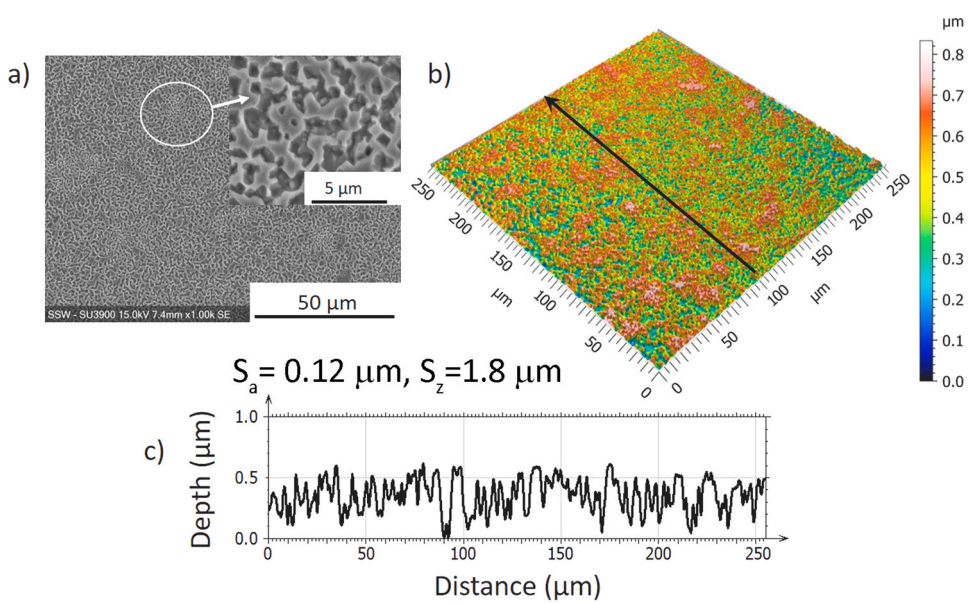

Fig. 13. Post-corrosion characterization of ED Cu: a) SEM image of the surface, b) CLSM 3D image, b) surface profile extracted from the location marked by the arrow.

and the establishment of a catalytic corrosion cycle.

Experiments involving large and small Cu surface area to solution volume (S_A/V) ratios demonstrated that for small S_A/V ratios the latter potential oxidants (Cu^{2+} and NO_2^-) could escape by transport to the bulk of solution, leading to their dilution at the Cu surface and limiting their involvement in the corrosion process. When the S_A/V ratio was large, such transport losses were limited and Cu corrosion accelerated by reactions (6) and (7).

This sequence of reactions offers an explanation for the promotion of corrosion occurring in the pores along particle boundaries of CS Cu, based on local S_A/V ratios. Initially, the O_2 reduction reaction would occur across the whole CS Cu surface. However, due to transport limitations, O_2 would become depleted within the pores and particle boundary fractures. By contrast, the NO_3^-, which in the present experiments was present at a significantly higher concentration than O_2, would not be similarly depleted in these regions. Combined with the mass transport restrictions, and the high solubility of Cu^+ in acidic solution, this would allow Cu^+ and the other potential oxidants (Cu^{2+} and NO_2^-) to accumulate in these high S_A/V ratio locations, initiating the catalytic corrosion cycle locally, particularly reactions (4), (6) and (7). Conversely, on the boldly exposed surfaces, where S_A/V ratios are smaller, Cu^{2+} and NO_2^- could escape by transport to the bulk of solution, meaning corrosion on these surfaces would be directly driven by oxygen but not by the catalytic cycle. This would lead to more rapid corrosion within pores and fractures at particle boundaries than on the open surfaces. It also suggests the possibility of developing differential O_2 concentration cells between open surfaces and particle boundary pores and fractures. The presence of oxides at these locations in the form

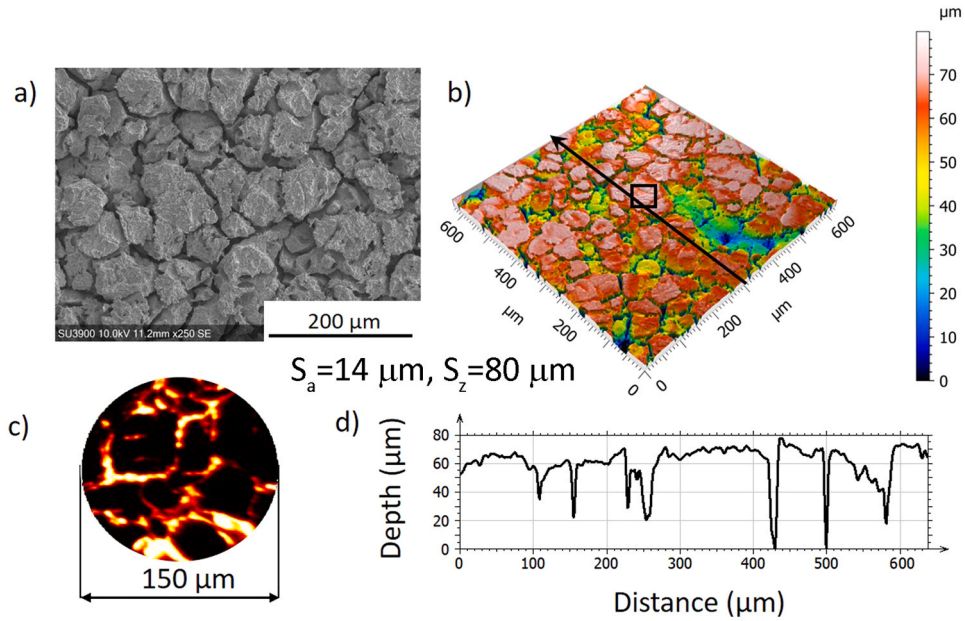

Fig. 14. Post-corrosion characterization of CS Cu: a) SEM image, b) 3D CLSM image, c) D-SIMS elemental map for ^{16}O, d) surface profile extracted from the area marked by the arrow in panel b.

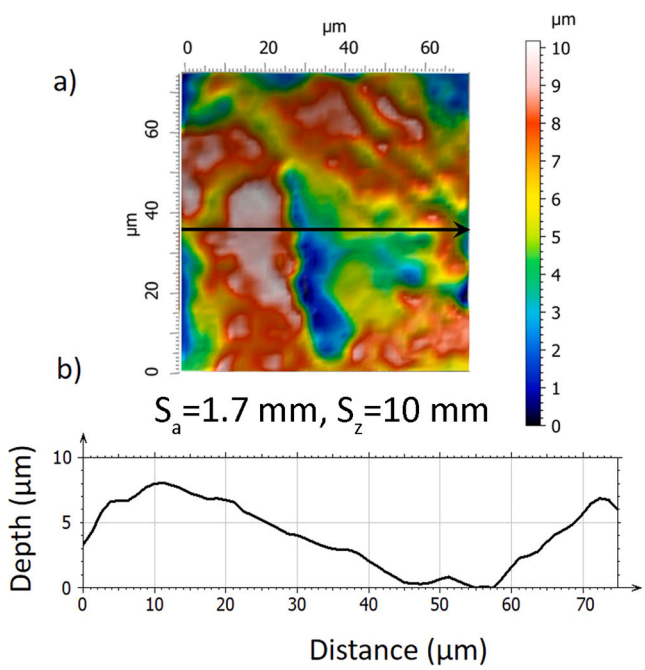

Fig. 15. Post-corrosion characterization of the area extracted from the particle of CS Cu marked by the black square in Fig. 14b: a) 3D CLSM image, b) surface profile extracted from the area marked by the arrow.

of either Cu_2O or CuO would not be expected to inhibit corrosion since they would dissolve in the acidic solution to produce Cu^+ and/or Cu^{2+} both of which would accelerate the localized corrosion by reactions (4) and (7).

6. Conclusions

- In this work, different Cu specimens were exposed to an aerated nitric acid solution to allow us to observe an accelerated corrosion of Cu in a short period of time, and to understand the reactivity of different grain structures under an aggressive condition.
- On the coarse-grained materials investigated (SKB Cu, ETP Cu, CW Cu) the corrosion behaviour was controlled by the crystallographic orientation of grains, with differently oriented grains corroding at different rates.
- On SKB Cu, the HAGBs corroded at a higher rate than did the grain surfaces, whereas preferential dissolution of grain boundaries was not prevalent on ETP Cu and CW Cu.
- On the refined-grained ED Cu, the corrosion rate was considerably lower than on the coarse-grained materials, with corrosion damage accumulating predominantly in the HAGBs.
- The corrosion rate in 100 mM nitric acid was considerably higher on CS Cu than on the coarse-grained materials, with corrosion progressing most rapidly within pores and along deposited particle boundaries. The propagation of corrosion within these locations was likely enhanced by the confinement of Cu^+, as well as oxidants NO_2^-

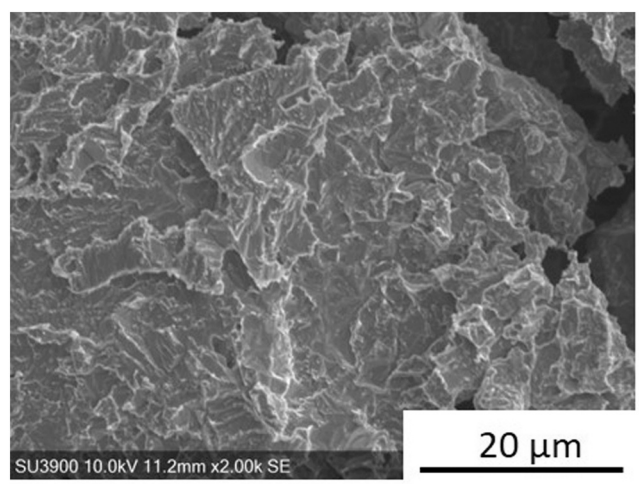

Fig. 16. SEM image showing corrosion damage in a particle interior in CS Cu after immersion for 24 h in aerated 100 mM HNO_3.

and Cu^{2+} produced by the reaction of NO_3^- with Cu^+, giving rise to a catalytic corrosion cycle locally.

Further investigations are underway to elucidate the influence of O in oxides present on the particle boundaries of CS Cu on its corrosion behaviour.

CRediT authorship contribution statement

Anna Dobkowska: Conceptualization, Formal analysis, Investigation, Methodology, Visualization, Writing – original draft, Writing – review & editing. **Millicent Dayle H. Castillo:** Investigation. **Joseph P. Turnbull:** Methodology. **Sridhar Ramamurthy:** Data curation, Project administration. **Dmitrij Zagidulin:** Data curation, Software. **Desmond E. Moser:** Funding acquisition, Writing – review & editing. **Mehran Behazin:** Funding acquisition, Writing – review & editing. **Peter G. Keech:** Funding acquisition, Writing – review & editing. **David W. Shoesmith:** Validation, Supervision, Writing – review & editing. **James J. Noël:** Supervision, Funding acquisition, Validation, Project administration, Writing – review & editing.

Declaration of Competing Interest

The authors declare that they have no known competing financial interests or personal relationships that could have appeared to influence the work reported in this paper.

Acknowledgements

This research was mainly funded by the Nuclear Waste Management Organization (Toronto, Canada) with minor support from an NSERC Discovery Grant to Desmond E. Moser. The authors are grateful to Mr. Gary Good (Surface Science Western, ON, Canada) for his support in D-SIMS measurements, Mr. Ivan Barker (Surface Science Western, ON, Canada) for support with SEM imaging of CS Cu, and Dr. Brendt Hyde (Zircon and Accessory Phase Laboratory, University of Western Ontario, ON, Canada) for assistance with SEM-EBSD measurements.

References

[1] A. Pardo, M.C. Merino, A.E. Coy, R. Arrabal, F. Viejo, E. Matykina, Corrosion behaviour of magnesium/aluminium alloys in 3.5wt% NaCl, Corros. Sci. 50 (2008) 823–834, https://doi.org/10.1016/j.corsci.2007.11.005.
[2] G. Ben Hamu, D. Eliezer, L. Wagner, The relation between severe plastic deformation microstructure and corrosion behavior of AZ31 magnesium alloy, J. Alloy. Compd. 468 (2009) 222–229, https://doi.org/10.1016/j.jallcom.2008.01.084.
[3] G. Meng, Y. Li, Y. Shao, T. Zhang, Y. Wang, F. Wang, X. Cheng, C. Dong, X. Li, Effect of microstructures on corrosion behavior of nickel coatings: (I) abnormal grain size effect on corrosion behavior, J. Mater. Sci. Technol. 31 (2015) 1186–1192, https://doi.org/10.1016/j.jmst.2015.10.011.
[4] M. Alvarez-Lopez, M.D. Pereda, J.A. Del Valle, M. Fernandez-Lorenzo, M.C. Garcia-Alonso, O.A. Ruano, M.L. Escudero, Corrosion behaviour of AZ31 magnesium alloy with different grain sizes in simulated biological fluids, Acta Biomater. 6 (2010) 1763–1771, https://doi.org/10.1016/j.actbio.2009.04.041.
[5] R. Ly, K.T. Hartwig, H. Castaneda, Influence of dynamic recrystallization and shear banding on the localized corrosion of severely deformed Al–Mg–Si alloy, Materialia 4 (2018) 457–465, https://doi.org/10.1016/j.mtla.2018.11.005.
[6] T.A.-S.S.S. Nenea, B.P. Kashyapa, N. Prabhua, Y. Estrina, Microstructure refinement and its effect on specific strength and bio-corrosion resistance in ultralight Mg–4Li–1Ca (LC41) alloy by hot rolling, J. Alloy. Compd. 615 (2014) 501–506.
[7] H.S. Kim, G.H. Kim, H. Kim, W.J. Kim, Enhanced corrosion resistance of high strength Mg-3Al-1Zn alloy sheets with ultrafine grains in a phosphate-buffered saline solution, Corros. Sci. 74 (2013) 139–148, https://doi.org/10.1016/j.corsci.2013.04.035.
[8] G.R. Argade, S.K. Panigrahi, R.S. Mishra, Effects of grain size on the corrosion resistance of wrought magnesium alloys containing neodymium, Corros. Sci. 58 (2012) 145–151, https://doi.org/10.1016/j.corsci.2012.01.021.
[9] H. Miyamoto, K. Harada, T. Mimaki, A. Vinogradov, S. Hashimoto, Corrosion of ultra-fine grained copper fabricated by equal-channel angular pressing, Corros. Sci. 50 (2008) 1215–1220, https://doi.org/10.1016/j.corsci.2008.01.024.
[10] L. Beaunier, Corrosion of grain boundaries: initiation processes and testing, J. Phys. (Paris) Colloq. 43 (1982) 271–282, https://doi.org/10.1051/jphyscol:1982624.
[11] L. Beaunier, M. Froment, C. Vignaud, A kinetical model for the electrochemical grooving of grain boundaries, Electrochim. Acta 25 (1980) 1239–1246, https://doi.org/10.1016/0013-4686(80)87127-1.
[12] K.D. Ralston, N. Birbilis, C.H.J. Davies, Revealing the relationship between grain size and corrosion rate of metals, Scr. Mater. 63 (2010) 1201–1204, https://doi.org/10.1016/j.scriptamat.2010.08.035.
[13] L. Lapeire, E. Martinez Lombardia, I. De Graeve, H. Terryn, K. Verbeken, Influence of grain size on the electrochemical behavior of pure copper, J. Mater. Sci. 52 (2017) 1501–1510, https://doi.org/10.1007/s10853-016-0445-z.
[14] R. Mishra, R. Balasubramaniam, Effect of nanocrystalline grain size on the electrochemical and corrosion behavior of nickel, Corros. Sci. 46 (2004) 3019–3029, https://doi.org/10.1016/j.corsci.2004.04.007.
[15] K.D. Ralston, D. Fabijanic, N. Birbilis, Effect of grain size on corrosion of high purity aluminium, Electrochim. Acta 56 (2011) 1729–1736, https://doi.org/10.1016/j.electacta.2010.09.023.
[16] M. Orłowska, E. Ura-Bińczyk, L. Olejnik, M. Lewandowska, The effect of grain size and grain boundary misorientation on the corrosion resistance of commercially pure aluminium, Corros. Sci. 148 (2019) 57–70, https://doi.org/10.1016/j.corsci.2018.11.035.
[17] J.K. Yu, E.H. Han, L. Lu, X.J. Wei, M. Leung, Corrosion behaviors of nanocrystalline and conventional polycrystalline copper, J. Mater. Sci. 40 (2005) 1019–1022, https://doi.org/10.1007/s10853-005-6524-1.
[18] A.V. Syugaev, E.A. Pechina, N.V. Lyalina, S.F. Lomaeva, M.V. Mar'in, S. M. Reshetnikov, The influence of the ultrafine-grained structure on passivation of copper, Prot. Met. Phys. Chem. Surf. 50 (2014) 841–845, https://doi.org/10.1134/S2070205114070168.
[19] K.D. Ralston, N. Birbilis, Effect of grain size on corrosion, Corrosion 66 (2010) 1–4, https://doi.org/10.5006/1.3462912.
[20] R. Rofagha, R. Langer, A.M. El-Sherik, U. Erb, G. Palumbo, K.T. Aust, The corrosion behaviour of nanocrystalline nickel, Scr. Metall. Mater. 25 (1991) 2867–2872, https://doi.org/10.1016/0956-716X(91)90171-V.
[21] N.N. Aung, W. Zhou, Effect of grain size and twins on corrosion behaviour of AZ31B magnesium alloy, Corros. Sci. 52 (2010) 589–594, https://doi.org/10.1016/j.corsci.2009.10.018.
[22] S. Gollapudi, Grain size distribution effects on the corrosion behaviour of materials, Corros. Sci. 62 (2012) 90–94, https://doi.org/10.1016/j.corsci.2012.04.040.
[23] E. Martinez-Lombardia, Y. Gonzalez-Garcia, L. Lapeire, I. De Graeve, K. Verbeken, L. Kestens, J.M.C. Mol, H. Terryn, Scanning electrochemical microscopy to study the effect of crystallographic orientation on the electrochemical activity of pure copper, Electrochim. Acta 116 (2014) 89–96, https://doi.org/10.1016/j.electacta.2013.11.048.
[24] L. Lapeire, E. Martinez Lombardia, K. Verbeken, I. De Graeve, L.A.I. Kestens, H. Terryn, Effect of neighboring grains on the microscopic corrosion behavior of a grain in polycrystalline copper, Corros. Sci. 67 (2013) 179–183, https://doi.org/10.1016/j.corsci.2012.10.017.
[25] A. Schreiber, J.W. Schultze, M.M. Lohrengel, F. Kármán, E. Kálmán, Grain dependent electrochemical investigations on pure iron in acetate buffer pH 6.0, Electrochim. Acta 51 (2006) 2625–2630, https://doi.org/10.1016/j.electacta.2005.07.052.
[26] E. Martinez-Lombardia, L. Lapeire, I. De Graeve, K. Verbeken, L.A.I. Kestens, H. Terryn, Study of the influence of the microstructure on the corrosion properties of pure copper, Mater. Corros. 67 (2016) 847–856, https://doi.org/10.1002/maco.201508719.
[27] H. Chen, V. Maurice, L.H. Klein, L. Lapeire, K. Verbeken, H. Terryn, P. Marcus, Grain boundary passivation studied by in situ scanning tunneling microscopy on microcrystalline copper, J. Solid State Electrochem. 19 (2015) 3501–3509, https://doi.org/10.1007/s10008-015-2787-x.
[28] B. Davepon, J.W. Schultze, U. König, C. Rosenkranz, Crystallographic orientation of single grains of polycrystalline titanium and their influence on electrochemical processes, Surf. Coat. Technol. 169–170 (2003) 85–90, https://doi.org/10.1016/S0257-8972(03)00163-4.
[29] M. Koralnik, A. Dobkowska, B. Adamczyk-Cieslak, J. Mizera, The influence of the microstructural evolution on the corrosion resistance of cold drawn copper single crystals in NaCl, Arch. Metall. Mater. 65 (2020) 55–64, https://doi.org/10.24425/amm.2019.131096.
[30] Z. Pu, G.L. Song, S. Yang, J.C. Outeiro, O.W. Dillon, D.A. Puleo, I.S. Jawahir, Grain refined and basal textured surface produced by burnishing for improved corrosion performance of AZ31B Mg alloy, Corros. Sci. 57 (2012) 192–201, https://doi.org/10.1016/j.corsci.2011.12.018.
[31] M. Liu, D. Qiu, M.C. Zhao, G. Song, A. Atrens, The effect of crystallographic orientation on the active corrosion of pure magnesium, Scr. Mater. 58 (2008) 421–424, https://doi.org/10.1016/j.scriptamat.2007.10.027.
[32] A. Chojnacka, J. Kawalko, H. Koscielny, J. Guspiel, A. Drewienkiewicz, M. Bieda, W. Pachla, M. Kulczyk, K. Sztwiertnia, E. Beltowska-Lehman, Corrosion anisotropy of titanium deformed by the hydrostatic extrusion, Appl. Surf. Sci. 426 (2017) 987–994, https://doi.org/10.1016/j.apsusc.2017.07.231.
[33] E.M. Lehockey, A.M. Brennenstuhl, I. Thompson, On the relationship between grain boundary connectivity, coincident site lattice boundaries, and intergranular stress corrosion cracking, Corros. Sci. 46 (2004) 2383–2404, https://doi.org/10.1016/j.corsci.2004.01.019.
[34] G. Palumbo, E.M. Lehockey, P. Lin, U. Erb, K.T. Aust, A grain boundary engineering approach to materials reliability, MRS Proc. 458 (1996) 273, https://doi.org/10.1557/PROC-458-273.
[35] Y. Yuan, Y. Jiang, J. Zhou, G. Liu, X. Ren, Influence of grain boundary character distribution and random high angle grain boundaries networks on intergranular

corrosion in high purity copper, Mater. Lett. 253 (2019) 424–426, https://doi.org/10.1016/j.matlet.2019.07.125.
[36] S. Xia, H. Li, T.G. Liu, B.X. Zhou, Appling grain boundary engineering to Alloy 690 tube for enhancing intergranular corrosion resistance, J. Nucl. Mater. 416 (2011) 303–310, https://doi.org/10.1016/j.jnucmat.2011.06.017.
[37] A. Lin, E.E. Hoffman, L.D. Marks, Effects of grain boundary misorientation and chromium segregation on corrosion of CoCrMo alloys, Corrosion 73 (2017) 256–267, https://doi.org/10.5006/2233.
[38] T.E. Standish. Galvanic Corrosion of Copper-coated Carbon Steel for Used Nuclear Fuel Containers, The University of Western Ontario, 2019. ⟨https://ir.lib.uwo.ca/etd/6705⟩.
[39] R. Crowe, K. Birch, J. Freire-Canosa, J. Chen, D. Doyle, F. Garisto, P. Giersewski, M. Gobien, C. Hatton, N. Hunt, S. Hirchorn, M. Hobbs, M. Jensen, P. Keech, L. Kennell, E. Kremer, P. Maak, J. Mckelvie, C. Medri, M. Mielcarek, A. Murchison, A. Parmenter, R. Ross, E. Sykes, T. Yang, Technical Program for Long-Term Management of Canada' s Used Nuclear Fuel – Annual Report 2013, 2015.
[40] NWMO Report, Description of a Deep Geological Repository and Centre of Expertise for Canada ' s Used Nuclear Fuel, 2015.
[41] N. Giroud, Y. Tomonaga, P. Wersin, S. Briggs, F. King, T. Vogt, N. Diomidis, On the fate of oxygen in a spent fuel emplacement drift in Opalinus Clay, Appl. Geochem. 97 (2018) 270–278, https://doi.org/10.1016/j.apgeochem.2018.08.011.
[42] T. Standish, J. Chen, R. Jacklin, P. Jakupi, S. Ramamurthy, D. Zagidulin, P. Keech, D. Shoesmith, Corrosion of copper-coated steel high level nuclear waste containers under permanent disposal conditions, Electrochim. Acta 211 (2016) 331–342, https://doi.org/10.1016/j.electacta.2016.05.135.
[43] P. Jakupi, P.G. Keech, I. Barker, S. Ramamurthy, R.L. Jacklin, D.W. Shoesmith, D. E. Moser, Characterization of commercially cold sprayed copper coatings and determination of the effects of impacting copper powder velocities, J. Nucl. Mater. 466 (2015) 1–11, https://doi.org/10.1016/j.jnucmat.2015.07.001.
[44] T.E. Standish, D. Zagidulin, S. Ramamurthy, P.G. Keech, D.W. Shoesmith, J.J. Noël, Synchrotron-based micro-CT investigation of oxic corrosion of copper-coated carbon steel for potential use in a deep geological repository for used nuclear fuel, Geosciences 8 (2018) 360, https://doi.org/10.3390/geosciences8100360.
[45] P.G. Keech, P. Vo, S. Ramamurthy, J. Chen, R. Jacklin, D.W. Shoesmith, Design and development of copper coatings for long term storage of used nuclear fuel, Corros. Eng. Sci. Technol. 49 (2014) 425–430, https://doi.org/10.1179/1743278214y.0000000206.
[46] X. Zhang, Development of the structural design basis of the long-term storage container for Canada's used nuclear fuel, in: 4th Can. Conf. Nucl. Waste Manag. Decommissioning Environ. Restor., 2013: pp. 37–41. ⟨doi:10.1080/02626667.2013.819433⟩.
[47] F. King, C. Lilja, K. Pedersen, P. Pitkänen, M. Vähänen, An update of the state-of-the-art report on the corrosion of copper under expected conditions in a deep geologic repository, Stockholm, 2010.
[48] D.S. Hall, M. Behazin, W.J. Binns, P.G. Keech, An evaluation of corrosion processes affecting copper-coated nuclear waste containers in a deep geological repository, Prog. Mater. Sci. 118 (2021), 100766, https://doi.org/10.1016/j.pmatsci.2020.100766.
[49] F. King, L. Ahonen, C. Taxen, U. Vuorinen, L. Werme, Copper corrosion under expected conditions in a deep geologic repository, 2001.
[50] R.P. Morco, J.M. Joseph, D.S. Hall, C. Medri, D.W. Shoesmith, J.C. Wren, Modelling of radiolytic production of HNO3relevant to corrosion of a used fuel container in deep geologic repository environments, Corros. Eng. Sci. Technol. 52 (2017) 141–147, https://doi.org/10.1080/1478422X.2017.1340227.
[51] J.P. Turnbull. The Influence of Radiolytically Produced Nitric Acid on the Corrosion Resistance of Copper-Coated Used Nuclear Fuel Containers, The University of Western Ontario,, 2020 doi:https://ir.lib.uwo.ca/etd/6903.
[52] J. Turnbull, R. Szukalo, D. Zagidulin, D.W. Shoesmith, Nitrite effects on copper corrosion in nitric acid solutions, Corros. Sci. 179 (2021), 109147, https://doi.org/10.1016/j.corsci.2020.109147.
[53] J. Turnbull, R. Szukalo, M. Behazin, D. Hall, D. Zagidulin, S. Ramamurthy, J. C. Wren, D.W. Shoesmith, The effects of cathodic reagent concentration and small solution volumes on the corrosion of copper in dilute nitric acid solutions, Corrosion 74 (2018) 326–336, https://doi.org/10.5006/2655.
[54] M. Wu, M. Behazin, J. Nam, P. Keech, R. Morco, Internal corrosion of used fuel container, 2019. ⟨https://www.nwmo.ca/~/media/Site/Reports/2019/02/25/22/45/NWMOTR201902–Internal-Corrosion-of-Used-Fuel-Container.ashx?la=en⟩.
[55] R.P. Morco, J.M. Joseph, D.S. Hall, C. Medri, D.W. Shoesmith, J.C. Wren, Modelling of radiolytic production of HNO3 relevant to corrosion of a used fuel container in deep geologic repository environments, Corros. Eng. Sci. Technol. 52 (2017) 141–147, https://doi.org/10.1080/1478422X.2017.1340227.
[56] ISO 25178–2: Geometrical product specifications (GPS) – Surface texture: Areal – Part 2: Terms, definitions and surface texture parameters, 2012.
[57] W. Li, B. Yu, J. Tam, J.D. Giallonardo, D. Doyle, D. Poirier, J.G. Legoux, P. Lin, G. Palumbo, U. Erb, Microstructural characterization of copper coatings in development for application to used nuclear fuel containers, J. Nucl. Mater. 532 (2020), 152039, https://doi.org/10.1016/j.jnucmat.2020.152039.
[58] C.H. Boyle, S.A. Meguid, Mechanical performance of integrally bonded copper coatings for the long term disposal of used nuclear fuel, Nucl. Eng. Des. 293 (2015) 403–412, https://doi.org/10.1016/j.nucengdes.2015.08.011.
[59] B. Yu, J. Tam, W. Li, H.J. Cho, J.G. Legoux, D. Poirier, J.D. Giallonardo, U. Erb, Microstructural and bulk properties evolution of cold-sprayed copper coatings after low temperature annealing, Materialia 7 (2019), 100356, https://doi.org/10.1016/j.mtla.2019.100356.
[60] J. Turnbull, R. Szukalo, D. Zagidulin, M. Biesinger, D. Shoesmith, The kinetics of copper corrosion in nitric acid, Mater. Corros. 72 (2021) 348–360, https://doi.org/10.1002/maco.202011707.
[61] S.-E. Bae, A.A. Gewirth, Differential reactivity of Cu(111) and Cu(100) during nitrate reduction in acid electrolyte, Faraday Discuss. 140 (2008) 113–123, https://doi.org/10.1039/b814058h.
[62] M. Maric, O. Muránsky, I. Karatchevtseva, T. Ungár, J. Hester, A. Studer, N. Scales, G. Ribárik, S. Primig, M.R. Hill, The effect of cold-rolling on the microstructure and corrosion behaviour of 316L alloy in FLiNaK molten salt, Corros. Sci. 142 (2018) 133–144, https://doi.org/10.1016/j.corsci.2018.07.006.
[63] U. Erb, H. Gleiter, G. Schwitzgebel, The effect of boundary structure (energy) on interfacial corrosion, Acta Met. 30 (1982) 1377–1380, https://doi.org/10.1016/0001-6160(82)90157-2.
[64] M. Yamashita, T. Mimaki, S. Hashimoto, S. Miura, Effect of interfacial structure and energy on corrosion and stress-corrosion-cracking in α Cu-Al alloy bicrystals, C1-715–C1-720, J. Phys. Colloq. 51 (1990), https://doi.org/10.1051/jphyscol:19901114.
[65] H. Miyamoto, T. Mimaki, A. Vinogradov, S. Hashimoto, Intergranular corrosion of ultrafine grain copper fabricated by ECAP, Mater. Sci. Forum 561–565 (2007) 2385–2388, https://doi.org/10.4028/www.scientific.net/MSF.561-565.2385.
[66] J. Turnbull, R. Szukalo, D. Zagidulin, M. Behazin, D.W. Shoesmith, Electronic cigarette use among patients with cancer: characteristics of electronic cigarette users and their smoking cessation outcomes (Erratum: Borderud SP, Li Y, Burkhalter JE, Sheffer CE and Ostroff JS), Cancer 121 (2015) 800, https://doi.org/10.1002/maco.202011707.